Supplementary information

1 Prediction and observations

The candidate star for the occultation analysed in this paper was discovered during a systematic search for candidate stars to be occulted by Pluto and other several large TNOs in 2008-15, conducted at the 2.2m telescope of the European Southern Observatory[15]. It revealed the star NOMAD1 0856-0015072 with $V \sim 17.1$, $R \sim 16.9$ as a potential candidate for an occultation by Eris on the night of 6 November 2010 around 02:20 UT. Initial possible zones of visibility included western Europe and Africa, as well as north and south America (see www.lesia.obspm.fr/perso/bruno-sicardy/predic_occn_10/Eris_2010). This was the unique event predicted for 2010. Actually, stellar occultations by Eris remain rare events as the dwarf planet moves far away from the galactic plane, in poor stellar fields in Cetus constellation (no event involving Eris is expected in our list before 2013).

Measurements made at the 2.2m telescope of the European Southern Observatory (see ref. 15 for the method) provide the following ICRF (loosely speaking J2000) star position as given by the UCAC2 reference frame:

$$\begin{cases} \alpha = 01^{h} \ 39^{min} \ 09.9421^{s} \\ \\ \delta = -04° \ 21' \ 12.119" \end{cases} \quad (1)$$

with 1σ errors of about 50 milli-arcsec (mas) in both right ascension and declination.

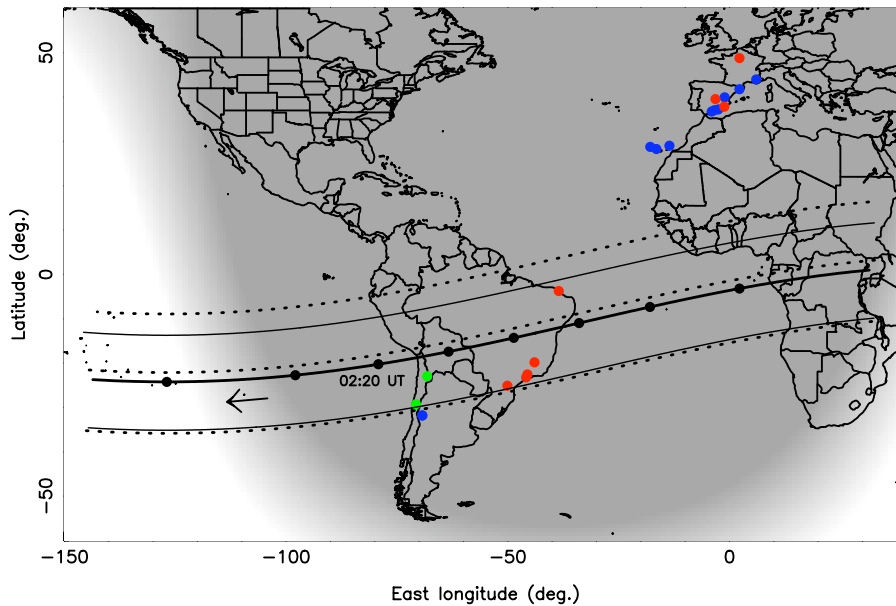Astrometric updates were conducted from October 18, 2010 onward to pin down the prediction

Figure 1S | The Eris observation campaign. The locations listed in Tables 1S-2S are plotted in green for the sites where the occultation was detected, in blue where observations were made but no occultation was observed and in red for stations with clouds. The three parallel dotted lines show the latest prediction (northern, central and southern limits of Eris' shadow) made about 24 hours before the event, assuming a radius of 1,500 km for the dwarf planet. The solid line with dots is the actual path of Eris' shadow centre derived from the solution shown in Fig. 2, with the dots plotted every minute (see the reference dot plotted at 02:20 UT, November 6, 2010) and the arrow shows the direction of motion on Earth. The other two parallel thinner solid lines are the shadow limits, using again the solution of Fig. 2 (radius 1,163 km).
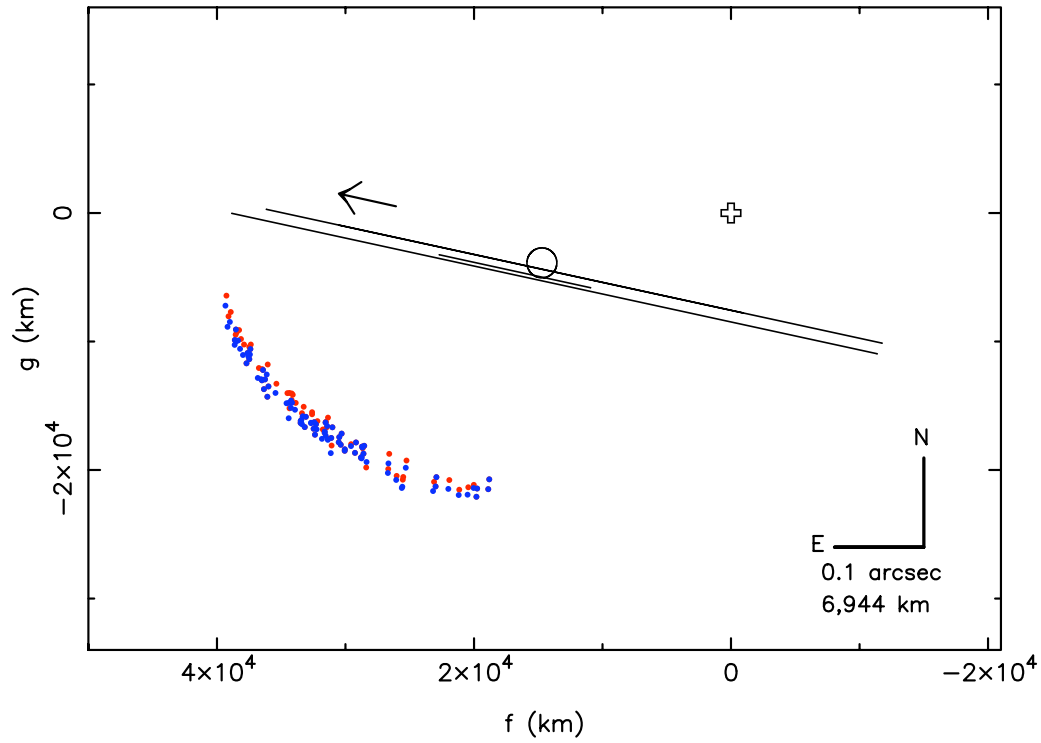
Figure 2S | Star motion with respect to Eris and Dysnomia. Oblique lines: the trajectories of the occulted star relative to Eris, as seen from San Pedro de Atacama, La Silla and CASLEO from top to bottom, respectively. Corresponding start and end times are provided in Table 1S. The arrow shows the direction of the stellar motion. Open cross: the expected Eris' centre position from our reference star position (Eq. 1) and the JPL28 ephemeris. Black circle: circular fit to the occultation chords, see Fig. 2. The shift between the cross and the circle is Eris' offset relative to JPL28, i.e. +211±50 mas and -56±50 mas in right ascension and declination, respectively, see Table 3S. Red (resp. blue) dots: expected position of Dysnomia at 02:20 UT (November 06, 2010) according to the Orbit 1 (resp. Orbit 2) orientation of Dysnomia's orbit[12]. The dots have been generated by using various possible orbital solutions that match Dysnomia observations. The scatter of the points shows the uncertainty on Dysnomia's position at the moment of occultation. Scale and orientation are given at lower right.

and organise the observational campaign, based on images taken at Calar Alto, Cerro Burek, Pico dos Dias and Table Mountain. Only after November 1st, 2010, was the position of Eris relative to the star accurate enough to clearly show that the event would be visible from south America, and possibly northern Africa and southern Europe.

Twenty six stations were eventually involved in our campaign, most of them being clouded out and/or outside the shadow path (Fig. 1S). The occultation was detected from two sites in Chile, one with two telescopes separated by about 20 meters (0.5m-Harlingten and 0.4m-ASH2) at San Pedro de Atacama (San Pedro for short), and the other one at the ESO La Silla site with the new 0.6m TRAnsiting Planets and PlanetesImals Small Telescope[27] (TRAPPIST). A third station in Argentina (Complejo Astronomico El Leoncito, CASLEO, 2.15-m Jorge Sahade telescope) was sufficiently close to the shadow edge (∼200 km, see Fig. 2 and 1S) and with a sufficient SNR to be used for potentially placing an upper limit of Eris' atmosphere. Table 1S provide details on the observations analysed here, while Table 2S lists all our other attempts made during that campaign.

The general geometry of the event is shown in Fig. 2S. Besides the Eris events detected at San Pedro and La Silla (see below), no secondary events were detected in the light curves that we have analysed. Note that Dysnomia predicted position was far away from the stellar tracks that scanned Eris' surrounding (Fig. 2S).

2 Data analysis

All data shown here were obtained with broadband (no filter) CCD images, in order to maximise photon flux. The camera types used at each telescope are given in the caption of Fig. 1. After classical dark subtraction and flat fieldings, aperture photometry was performed to derive the stellar flux vs. time. The aperture used for Harlingten was a square with size 4×4 pixels, while circles with diameters 4, 5 and 6 pixels were used for ASH2, TRAPPIST and Jorge Sahade, respectively. The background flux was estimated near each star and subtracted, so that the zero flux corresponds to the sky level. Images taken at the ASH2 and TRAPPIST telescopes the night after the event allowed us to estimate the fluxes from Eris at the moment of the occultation, see the dotted lines in Fig. 1 and Fig. 3S. This calibration shows that the star completely disappeared during the event, down to the noise level. A nearby reference star (NOMAD1 0856-0015078), roughly two magnitudes brighter than the target, was used to correct the stellar flux for low frequency sky transparency variations at La Silla and CASLEO. Due to the good conditions prevailing at San Pedro (with a target elevation of ∼68 degrees), this correction was not necessary. A further division by the unocculted stellar + Eris flux, averaged over several minutes around the occultation, eventually provides the normalised light curves presented in Figs. 1 and 3S. The flux statistics yields the standard deviation of the signal, which defines the 1σ error bar on each data point, used later for fitting diffraction models to the star disappearances and re-appearances, see below.

Supplementary Table 1S | Circumstances of observations for the data used in this paper

Site	Telescope aperture Integration/cycle times[a] Signal-to-noise ratio[b]	longitude latitude altitude	start end h:min:s	disappearance[c] re-appearance[c] h:min:s±s UT) (6 November 2010)	observers
San Pedro de Atacama	0.5m-Harlingten 3s/3.88s 19.2	68° 10' 47.6'' W 22° 57' 12.3'' S 2,397 m	02:09:17.7 02:29:20.8	02:18:41.6±0.15 02:19:59.4±0.18[d] 02:20:00.6±0.18[e]	A. Maury S. Saravia
San Pedro de Atacama	0.4m-ASH2 15s/18.32s 15.0	68° 10' 46.9'' W 22° 57' 12.2'' S 2,397 m	02:02:24.8 02:32:57.3	02:18:39.8±1.3 02:19:58.9±3.1	remotely operated by N. Morales & I. de la Cueva
La Silla	0.6m-TRAPPIST 3s/4.55s 40.2	70° 44' 21.8'' W 29° 15' 16.6'' S 2,315 m	02:16:58.8 02:24:29.4	02:19:17.1±0.11 02:19:48.4±0.10	remotely operated by E. Jehin
CASLEO	2.15m-Jorge Sahade 4s/7s 56.5	69° 17' 44.9'' W 31° 47' 55.6'' S 2,492 m	02:02:38.1 02:34:41.4	no occultation	R. Gil-Hutton

[a] All the observations listed here were made with fast broadband visible CCD, see Fig. 1.
[b] The ratio of the star plus Eris flux to the r.m.s. noise per data point.
[c] All error bars are at 1σ level.
[d] and [e] are solution 1 and solution 2 described in the text, respectively, for the star re-appearance at San Pedro, see text and Fig. 3S.

The UT time of each image was taken from the frame headers. However, for the three stations where the event was detected (Harlingten, ASH2 and TRAPPIST), only the integer part of the second is available, due to the truncated format provided by the MaximDL software used at those three stations. To retrieve the correct timing of each image, we fitted a linear model to the set of points $(i, t_{h,i})$, where i is the image number, and $t_{h,i}$ is the corresponding time written in the

Supplementary Table 2S | Circumstances of observations at other stations

Site	Telescope aperture	longitude latitude, altitude	Result	observers
Meudon	0.6m	02° 13' 53" E 48° 48' 18" N, 162 m	clouds	F. Braga-Ribas, F. Roques, B. Sicardy
Puimichel	1.0m	06° 01' 15" E 43° 58' 49" N, 700 m	no occ	F. Colas, J. Lecacheux
Esteve Duran	0.6m	02° 15' 32" E 41° 47' 57" N, 720 m	partly cloudy	E. García-Melendo
València	0.6m TROBAR	01° 06' 05" W 39° 56' 42" N, 1,271 m	partly cloudy	V. Peris, J. Fabregat
La Hita	0.77m	03° 41' 10" W 39° 34' 07" N, 675 m	clouds	F. Organero
La Murta	0.4m	01° 12' 10" W 37° 50' 25" N, 404 m	clouds	S. Pastor, J. A. de los Reyes
Calar Alto	0.5m CAB	02° 32' 45" W 37° 13' 25" N, 2,173 m	no occ	remotely operated by L. Cuesta
	1.2m		no occ	remotely operated by S. Mottola
	2.2m		no occ	S. Pedraz
Sierra Nevada	1.5m	03° 23' 05" W 37° 03' 51" N, 2,930 m	no occ	A. Sota
Málaga	0.6m Bootes-2/TELMA	04° 02' 33" W 36° 45' 30"N, 62 m	no occ	A. Castro R. Sánchez-Ramírez
Nazaret	0.3m	13° 33' 22" W 29° 02' 29" N, 366 m	no occ	G. Muller
La Palma	2m Liverpool	17° 52' 45" W 28° 45' 45" N, 2,321 m	no occ	remotely operated by I. A. Steele
Teide	0.8m IAC80	16° 29' 48" W 28° 17' 30" N, 2,112 m	no occ	M. Cebrián, A. Oscoz P. Montañés-Rodríguez
Fortaleza	0.3m	38° 30' 27" W 03° 44' 18" S, 38 m	clouds	D. Weaver
CEAMIG-REA	0.3m	43° 59' 51" W 19° 49' 49" S, 825 m	clouds	C. Jacques, E. Pimentel, B. Giacchini
Pico dos Dias	1.6m	45° 34' 58" W 22° 32' 08" S, 1,840 m	clouds	M. Assafin, W. Corradi, W. Reis Jr., F. P. Santos, A. Ramos Gomes Jr.
São José dos Campos	0.275m	45° 51' 44" W 23° 12' 33" S, 617 m	clouds	A. Milone
Ponta Grossa	0.4m	50° 05' 56" W 25° 05' 22" S, 909 m	clouds	M. Emilio
Cerro Burek	0.45m ASH	69° 18' 25" W 31° 47' 12" S, 2,665 m	no occ	remotely operated by N. Morales
Sevilla	0.3m	06° 19' 35" W 31° 40' 19" N, 471 m	no occ	J. M. Madiedo
San Pedro Mártir	1.5m	115° 27' 48" W 31° 02' 36" N, 2,825 m	no occ	L. Gutiérrez, H. Hernández-Toledo

header. The residuals of those fits, performed over intervals of several minutes around the event, show a regular sawtooth pattern confined between -0.5 and +0.5 seconds. This (1) confirms that the truncation to the integer part of the second is indeed present, and (2) shows that the acquisition cycle was regular. To obtain the mid-exposure time of each frame, we finally added to the fitted

times half of the total exposure time, plus a bias correction of $+0.5$ s to account for the truncation. The slope of the fit also provides the cycle time, and thus, the readout overhead (or 'dead time') between two frames by subtraction of the exposure time, see Table 1S. Note that this dead time leads to a net loss of information.

The internal accuracy of those linear fits ensures that the absolute times of individual images can be retrieved to better than 0.05 s. Furthermore, the computers used at San Pedro and La Silla were set up against UT time every 15 minutes at least, using a time server and the 'Dimension 4' synchronisation software, which ensures an absolute time accuracy better than 0.05 s for all computers. In summary, the time associated with each image has an absolute accuracy of about 0.07 s, corresponding to an accuracy of $\pm$ 2km along Eris' shadow track, which is negligible compared to the error associated with the model fitting described below.

3   Occultation timing

The star dis- and re-appearance times are obtained by fitting an abrupt edge shadow model to the light curves, after convolving that shadow by Fresnel diffraction, stellar diameter[28] projected at Eris, finite bandwith of the CCD and finite integration time of the instrument[29]. The final synthetic light curve is largely dominated by finite integration time, which was 3 s or more for all data sets, see Table 1S. At La Silla (resp. San Pedro), this corresponds to a distance of about 30 km (resp. 75 km) perpendicular to Eris' limb, while Fresnel's scale is about 2 km, and the star diameter projected at Eris is about 0.7 km. The free parameter of the fit is the time of star dis- or re-appearance, t_{occ}, i.e. the time at which the occultation would occur in the limit of a point source occulted by a sharp edge in the geometrical optics regime. The fit procedure looks for the minimum value χ^2_{min} of

$$\chi^2 = \sum_1^N (\Phi_{i,\mathrm{obs}} - \Phi_{i,\mathrm{cal}})^2 / \sigma_i^2, \qquad (2)$$

where $\Phi_{i,\mathrm{obs}}$ (resp. $\Phi_{i,\mathrm{cal}}$) is the observed (resp. calculated) flux at point i, σ_i is the 1σ error bar at that point, estimated as explained earlier, and N is the total number of points considered. The 1σ error bar on t_{occ} is estimated by varying t_{occ} so that to increase χ^2 from the best value χ^2_{min} to $\chi^2_{\mathrm{min}} + 1$.

The best fits are shown in Fig. 3S, and the corresponding occultation times are listed in Tables 1S and 3S. When adjusting the star re-appearance at San Pedro/Harlingten, two equally satisfactory fits (called solution 1 and solution 2, in chronological order) are obtained. This is because it occurred near one of the 0.88 s gaps between consecutive exposures (Table 1S). Consequently, the χ^2 residual exhibits two local minima for two values of t_{occ} separated by 1.2 s, corresponding to a difference of 32 km in the two chord lengths, see Fig. 3S and Table 3S.

4   Occultation geometry and Eris' size

The occultation times given in Table 3S provide the corresponding star positions (f, g) relative to Eris and projected in the plane of the sky, where f is the relative position in right ascension, positive if the star is east of Eris centre, and g is the relative position in declination, positive if the star is north of Eris centre. The quantities f and g are expressed in kilometers. For this calculation, we use the JPL28 geocentric Eris ephemeris (ref. 30 and http://ssd.jpl.nasa.gov/), corrected for parallax effects at each station. Note that due to the larger integration time (15 s) and lower signal

to noise ratio obtained at the San Pedro ASH2 telescope, compared to the Harlingen telescope (3 s integration time), the former data do not bring further constraints to the occultation length. Although they confirm the event (Fig. 3S), they are not included in the analysis below. So, we finally obtain four extremities of the two occultation segments (or 'chords'), derived from the timings at San Pedro/Harlingen and La Silla/TRAPPIST telescopes, see the red segments in Fig. 2.

The most general limb shape considered here is an ellipse projected in the plane of the sky, with
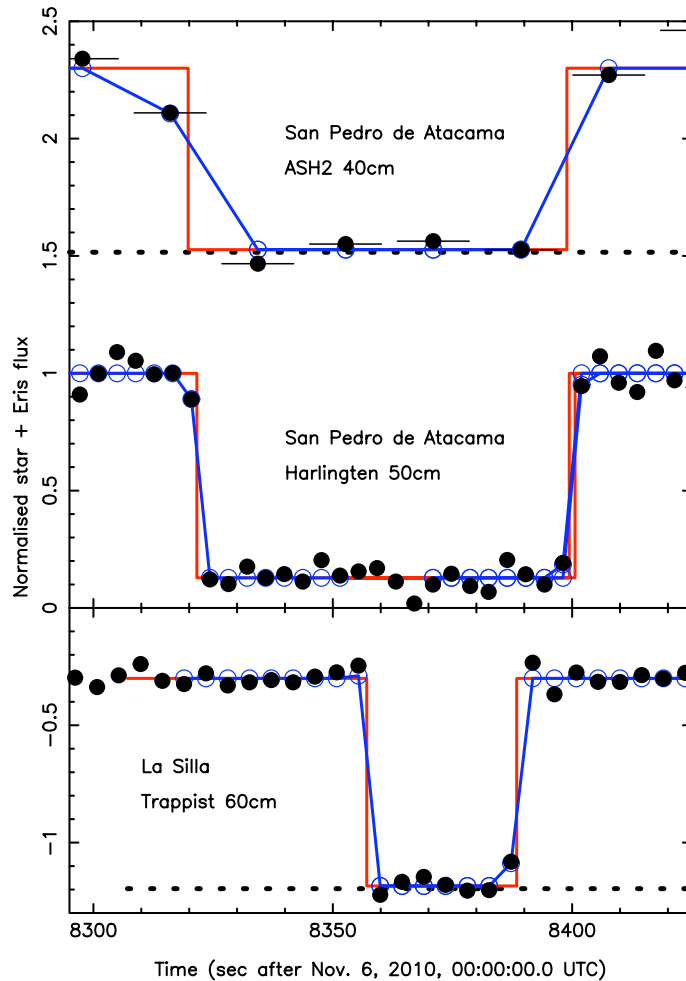

Figure 3S | Fitting diffraction models to the occultation light curves. Black bullets: the occultation data points obtained at the station mentioned in Table 1S (where the star plus Eris fluxes have been normalised to unity). Plots for ASH2 and TRAPPIST data have been shifted vertically by +1.3 and -1.3, respectively, for better viewing. The horizontal bars on the ASH2 data points show the acquisition time intervals corresponding to each point. For the Harlingen and the TRAPPIST data points, the bars have approximately the size of the bullets, and are not visible on the plot. Note that all data sets have 'dead times', i.e. intervals of time when no data are acquired, see Table 1S. The dotted lines under the ASH2 and the TRAPPIST light curves show Eris' contribution to the total flux (0.216 and 0.104, respectively), determined by measuring the occulted star against a nearby reference star the night after the occultation, with the same instrument setup and same airmass. Red curves: the best fit square-well models to the data (corresponding to Eris' shadow edge in the geometrical optics regime). Two equally satisfactory fits are obtained for the star re-appearance at San Pedro (the so-called solutions 1 and 2, from left to right, respectively, see text). Open blue circles: expected flux derived from the red model, and corresponding to each observed data point, once diffraction, star diameter, finite bandwith and finite acquisition time intervals have been accounted for. The open blue circles obtained with both solutions 1 and 2 have been plotted for the Harlingen telescope, but they are almost indistinguishable at the scale used here. The blue curve connects the open blue circles.

Supplementary Table 3S | Fits to the occultation chords[a]

site	6 November 2010 (h:min:s UT)	f[b] (km)	g[b] (km)	shadow velocity[c] (km s^{-1})	radial residual (km, circular fit) solution 1	solution 2
San Pedro, disappearance	02:18:41.6±0.15	+13782.9	-4575.6	26.748	+10.9	+2.4
San Pedro, re-appearance (sol1)	02:19:59.4±0.18	+15816.5	-4133.9	26.748	-16.3	–
San Pedro, re-appearance (sol2)	02:20:00.6±0.18	+15847.9	-4127.1	26.748	–	-3.4
La Silla, disappearance	02:19:17.1±0.11	+14538.7	-5026.2	26.723	-2.0	-0.4
La Silla, re-appearance	02:19:48.4±0.10	+15356.0	-4848.5	26.723	+2.0	+0.4

free parameters of circular fit		Best fit values
Eris' radius R_E (km)	1,141	1,163±6
Eris' centre[d] f_c (km)	+14,717	+14,716±3
Eris' centre[d] g_c (km)	-3,902	-3,877±10
Goodness of fit, χ^2_{pdf}[e]	30.7	1.38
Radial residual (km)[f]	9.88	2.11
Time of geocentric closest approach (h:min:s UT, 6 November 2010)[g]	02:18:15.7	02:18:15.9±0.1
Distance of closest approach to geocentre (km)[h]	1,246	1,223±10
Offset[i] in right ascension (mas) with respect to DE405/JPL28	+212±50	+212±50
Offset[i] in declination (mas) with respect to DE405/JPL28	-56±50	-56±50

[a] The timings from the San Pedro/0.4m-ASH2 telescope are not included in the fits, as their larger error bars do not bring further constraints on the length of the occultation at that site (Table 1S and Fig. 3S).

[b] The timings of Table 1S provide the star position relative to Eris expected centre, using the DE405/JPL28 Eris' ephemeris (http://ssd.jpl.nasa.gov). This position is projected in the plane of the sky, in km, where f is the relative position in right ascension, positive if the star is east of Eris' centre, and g is the relative position in declination, positive if the star is north of Eris' centre. We use the ICRF/J2000 star position given in Eq. 1.

[c] Velocity of Eris' shadow at the considered site, perpendicular to the observer-Eris line (equivalent to Eris velocity relative to the star, projected in the plane of the sky). The *radial* velocities with respect to the shadow edge (assuming a circular shape) are 9.7 and 24.4 km s^{-1} at La Silla and San Pedro, respectively.

[d] This centre corresponds to the offset to be applied to Eris' position in order to match the occultation chords (see the cross in Fig. 2). This offset is relative to the DE405/JPL28 Eris ephemeris, but also depends on the adopted star position given in Eq. 1.

[e] Value of minimum χ^2 per degree of freedom, see text.

[f] Defined as the r.m.s. of the four radial residuals.

[g] Time at which Eris and the star are the closest in the sky plane, as seen from the geocentre.

[h] Distance between Eris' centre and the star in the sky plane at closest approach, as seen from the geocentre. Conversion to mas can be made using an Eris observer range of 95.738 AU during the occultation, corresponding to a scale of 69.436 km per mas. At closest approach, Eris was at a position angle of 167.57 degrees relative to the star, in the J2000 reference frame, as seen from the geocentre.

[i] These values are derived from the values of f_c and g_c given above. The error bars are dominated by the uncertainties on the star position (±50 mas), not by the error bars of the circular fit to the occultation chords.

semiaxes $a'>b'$ and apparent flattening $\epsilon'=(a'-b')/a'$. In the small angular momentum regime, this shape results from the projection of an oblate Maclaurin spheroid with semiaxes $a=b>c$, where a and c are the equatorial and polar radii, respectively. The true flattening of the body is then $\epsilon=(a-c)/a$, and for small values of ϵ, the latter is related to the apparent flattening through[31] $\epsilon'\sim\epsilon\cdot\sin^2(\zeta)$ where ζ is the angle between the rotation c-axis and the line of sight ($\zeta=0$ corresponding to pole-on geometry). In that case, we assume that the spheroid is observed equator-on (so that its true flattening is $\epsilon=\epsilon'$), remembering that more general viewing geometries will result in true flattenings $\epsilon>\epsilon'$. In the large angular momentum regime, the shape results from an elongated triaxial Jacobi ellipsoid with semiaxes $a>b>c$. In that case, the ellipsoid has to be observed almost pole-on because no brightness variations larger than 1% are observed for the dwarf planet[13,14]. We finally define Eris' effective radius R_E as the radius of a disk that has the same apparent surface area as the actual

body, so that $R_E = \sqrt{a'b'}$.

Our problem has $M=5$ free parameters: the apparent semi-major axis a', the apparent flattening $\epsilon' = (a' - b')/a'$, the ellipse orientation in the sky (position angle P of the semi-minor axis, counted eastward from the local celestial north), and the two coordinates of its centre f_c, g_c. Note that it is sufficient to consider $0 \le P < 180$ degrees, as other values of P yield the same solutions by symmetry.

We fit the $N=4$ chord extremities by finding the minimum value χ^2_{min} of

$$\chi^2 = \sum_{1}^{N} \left[(f_{i,obs} - f_c)^2 + (g_{i,obs} - g_c)^2 \right] / \sigma^2_{i,r}, \tag{3}$$

where $(f_{i,obs}, g_{i,obs})$ are the coordinates of the chord extremities, and $\sigma_{i,r}$ are the corresponding radial uncertainties obtained by multiplying the 1σ uncertainties on the occultation times by the local star velocity perpendicular to Eris' limb. The 1σ error bar on R_E is obtained by exploring values of R_E (the other parameters being free) so as to change χ^2 from χ^2_{min} to $\chi^2_{min} + 1$. The value of χ^2 per degree of freedom for the best fit, χ^2_{pdf} (see Table 3S) is given by $\chi^2_{pdf} = \chi^2_{min}/(N - M)$. With $N=4$ chord extremities, and $M=5$ free parameters, there is an infinity of possible solutions and χ^2_{pdf} is not defined. In order to obtain a preferred solution, we have to rely on independent observations and on physical arguments.

4.1 Circular fit

We first note in Fig. 2 that the two chords have almost the same median lines, i.e. the lines going through the middle of the segments, and perpendicular to them, see the blue line in Fig. 2. More precisely, the two median lines are separated by 21 km for solution 1, and 5 km for solution 2. Consequently, a circle can be fitted to the two chords to within our error bars, especially for solution 2.

This strongly suggests that Eris is indeed close to spherical, unless a very special geometry occurred, as discussed later. A circular fit has $M=3$ free parameters ($R_E = a' = b'$, f_c and g_c), so that $N - M = 1$ and $\chi^2_{pdf} = \chi^2_{min}$. Table 3S gives the values of R_E, f_c and g_c corresponding to the best fits using solutions 1 and 2, respectively. Note that due to the high value of χ^2_{pdf} in the case of solution 1, we do not provide error bars, since the assumption of a circular limb is not valid in this case, see main text. For solution 2, we obtain a radius $R_E = 1{,}163 \pm 6$ km for the best circular fit to the chords extremities. The position of Eris' centre, (f_c, g_c) corresponds to the offset to apply to Eris ephemeris in order to fit the occultation chords (Fig. 2). Note that since we actually determine Eris' position relative to the star at a given moment, this offset depends (1) upon the adopted ephemeris (here DE405/JPL28) and (2) upon the adopted star position (Eq. 1). Thus, if one uses an ephemeris different from JPL28 for Eris and/or a star position different from the one mentioned here, the offset should be corrected, taking into account both the differences between the ephemerides and star positions.

Using the star position in Eq. 1 and the ephemeris DE405/JPL28, we obtain offsets of $+212 \pm 50$ and -56 ± 50 mas for Eris, in right ascension and declination, respectively, where the error bar is dominated by the uncertainty in the star position. Alternatively, one may use the time and distance of geocentric closest approach (C/A) in the plane of the sky to calculate those offsets (see Table 3S), once a star position and a reference ephemeris is given, knowing that Eris was at a position angle of 167.57 degrees relative to the star at C/A, as seen from the geocentre.

4.2 Topographic features

Even if globally spherical, a body composed of compact ice with Eris' size may sustain small reliefs with maximum amplitude of typically $\lesssim \pm 5$ km (ref. 32). They may create randomly distributed local, radial limb distortions, thus altering the occultation chord lengths, and finally, the retrieved Eris' radius. However, ±5km corrugations are probably too high in the case of Eris. First, Eris' interior has a density of ~2.5 g cm^{-3} (see main paper), more than twice the density of ice, resulting in a surface gravity larger than for a pure ice body. Second, the low thermal inertia of TNOs[25,26] suggests low conductivity, porous surfaces that are unlikely to support large reliefs. We also note that other icy bodies like the Uranian satellite Titania (radius 789 km) have local topographic features of ±2 km at most (see the discussion in ref. 29). Another large icy satellite, Triton (radius 1,353 km), has even smaller reliefs, with amplitude of less than ~0.5 km (ref. 33)

We thus consider that an amplitude of ±3 km is a safe maximum for local topographic features on Eris' surface. Generating circular fits to the chords obtained with solution 2, and allowing for residuals up to 3 km, we obtain values of R_E in the range 1,163±6 km. This error bar may be combined quadratically with the formal error bar of ±6 km found above, yielding a final error bar of ±9 km for Eris' radius, in the circular limb assumption with (probably overestimated) reliefs of ±3 km.

4.3 Elliptical fit

As mentioned earlier, we can fit an infinity of elliptical limbs to the two occultation chords. If Dysnomia orbits in Eris' equatorial plane, then the limb orientation is determined and its position angle P can be fixed, see the next subsection. If this is not the case, and since we are primarily interested in Eris' effective radius, we want at least to estimate a plausible range of values for R_E.

To do so, we have fitted the two occultation chords with elliptical models where P and a' have been fixed to prescribed values. The free parameters of the fits are then ϵ', f_c and g_c, each best fit returning a value for R_E and providing a radial residual which indicates the quality of that fit. We have varied P between 0 and 180 degrees by steps of 1 degree, and a' between 1,000 and 1,800 km by steps of 10 km, first using the chords derived from solution 1, and then, from solution 2. Moreover, we have retained only the fits with radial residuals smaller than 4.2 km, which result from the quadratic addition of possible timing errors (corresponding to about ±3 km in radial direction) and/or topographic features on Eris' surface (with amplitude of about ±3 km, see above).

The results are summarised in Fig. 4S. The histogram of derived R_E's reaches a maximum near 1,165 km, as expected because it is close to the value derived from the circular fit, 1,163 km. The distribution rapidly drops as R_E deviates from that value. This is because elongated limb shapes require a fine tuning of P in order to go through the chord extremities, resulting in low probability of realisation, see Fig. 2. The 68.3% probability of occurrence centered around the maximum of the distribution (roughly corresponding to the usual 1σ level error bar for a normal distribution) corresponds to the interval R_E=1,165±90 km.

However, we note in Fig. 4S that the limb apparent flattening ϵ' rapidly increases as R_E deviates from 1,165 km, with a strong correlation betwen R_E and ϵ'. At the boundaries of the interval R_E=1,165±90 km, ϵ' reaches about 0.08, implying that the true flattening $\epsilon\sim\epsilon/\sin^2(\zeta)$ is even larger, as mentioned at the beginning of this section.

We can relate ϵ to the body spin frequency ω, assuming hydrostatic equilibrium. In the low angular momentum regime, the corresponding oblate Maclaurin spheroid with equatorial and polar radii a
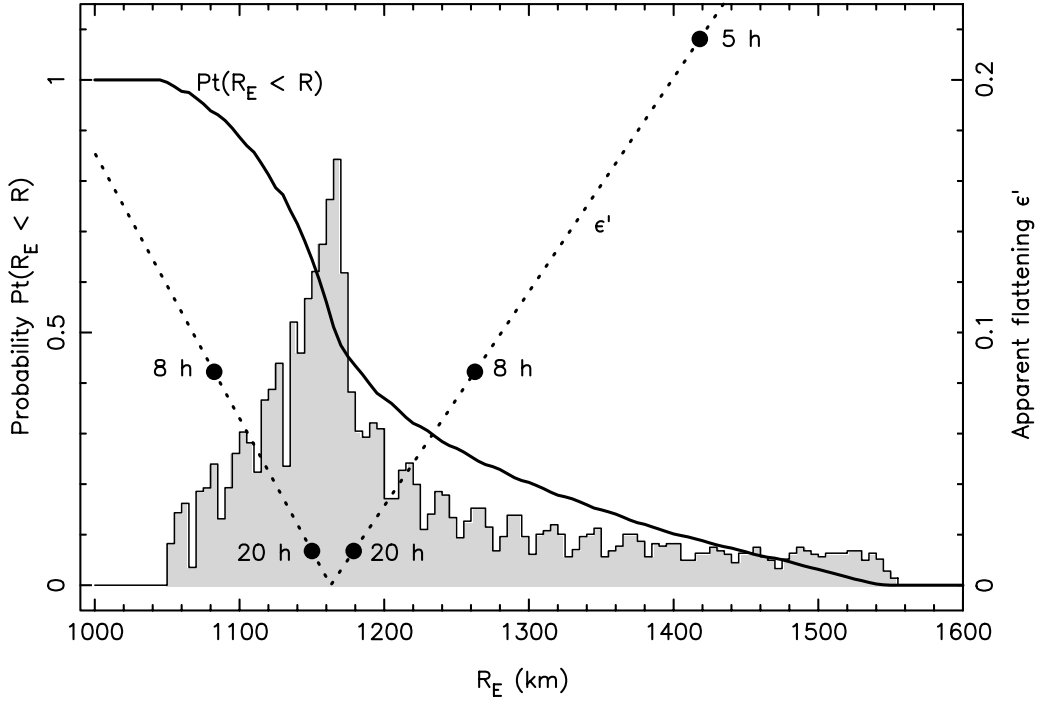
Figure 4S | Distribution of possible Eris' effective radius. Shaded surface: histogram, or probability density (arbitrary units), of Eris' effective radius R_E, derived from a wide variety of fits using elliptic limb models, see text. The integral of that histogram, starting from the right, is the probability $Pt(R_E < R)$ that R_E is larger than a given value R (thick solid line), see scale at left. The dotted line is the approximate correlation relation between R_E and the apparent flattening ϵ' obtained in the fits, see scale at right. The median of the distribution, $Pt(R_E < R)=0.5$, corresponds to $R_E \sim 1{,}165$ km, which is close to the circular fit value for solution 2, $R_E=1{,}163$ km. Approximate values (see Eq. 5) for the rotation periods corresponding to a few values of ϵ' are shown near the dotted lines, see the black bullets.

and c, respectively, must satisfy[34]:

$$\frac{\omega^2 a^3}{GM} = \frac{3\left\{2\psi\left[2 + \cos(2\psi)\right] - 3\sin(2\psi)\right\}}{4\sin^3(\psi)}, \tag{4}$$

where G is the gravitational constant, M is the mass of the body, and $\cos(\psi)=c/a=1-\epsilon$. Note that this equation assumes that the object is incompressible (uniform density). If compressible, complications arise and the body will rotate with slightly different periods. For small flattenings ϵ, Eq. 4 provides the approximation $\omega^2 a^3/GM \sim 4\epsilon/5$, yielding a rotation period of:

$$T = 2\pi/\omega \sim 2.33/\sqrt{\epsilon} \text{ hours}, \tag{5}$$

taking $a=1{,}163$ km and $M=(1.66\pm0.02)\times10^{22}$ kg (ref. 12).

For $\epsilon > \epsilon' \sim 0.08$, we obtain $T < 8.2$ hours. In other words, values of R_E outside the interval $1{,}165\pm90$ km require a fast rotating Eris. Rotation periods (more precisely, their upper bounds, as $\epsilon > \epsilon'$) corresponding to a few values of ϵ' are shown in Fig. 4S. They show that the required rotation period rapidly decreases as R_E deviates from 1,165 km, i.e. Eris must be a faster and faster rotator.

We may consider more extreme situations. For instance in Fig. 2, we may reconcile our results with IRAM flux[11] (yielding $R_E=1{,}500$ km) by considering a very elongated limb with $b'/a'=0.771$ (and $a'=1708$ km, $\epsilon'=0.229$). This can be achieved with a fast rotator, where Eris has a triaxial shape (Jacobi ellipsoid) with semiaxes $a>b>c$, observed pole-on to avoid rotational light curve. The ratios

$\beta=b/a=b'/a'$ and $\gamma=c/a$ are related to ω and M through:

$$\beta^2 \int_0^\infty \frac{du}{(1+u)(\beta^2+u)\Delta(\beta,\gamma,u)} = \gamma^2 \int_0^\infty \frac{du}{(\gamma^2+u)\Delta(\beta,\gamma,u)} \qquad (6)$$

$$\frac{\omega^2 a^3}{GM} = \frac{3}{2} \int_0^\infty \frac{udu}{(1+u)(\beta^2+u)\Delta(\beta,\gamma,u)}, \qquad (7)$$

where $\Delta(\beta,\gamma,u)=[(1+u)(\beta^2+u)(\gamma^2+u)]^{1/2}$, see e.g. ref. 17, noting the misprint in their Eq. 2, where the term Δ is missing in the denominator. Once $\beta=b/a$ is given, Eq. 6 yields γ, which in turn allows to calculate ω, using Eq. 7. In the example given in Fig. 2, we have $\beta=0.771$, from which we derive $\gamma=0.506$, and then a rotation period of 4.4 hours, i.e. a very fast rotator.

In this case, the long axis of the object should be perpendicular to the chords to within ± 2 degrees in order to keep the radial residuals of the fit under 4.2 km, as explained at the beginning of this subsection. This has a low probability of $\sim 2\%$ to occur for P randomly distributed between 0 and 180 degrees.

Moreover, Eris must be observed close to pole-on in this case, to avoid a rotational light curve. The light curve amplitude of such an object is, in magnitude[35]:

$$\Delta m = -1.25 \cdot \log_{10}\left[\frac{1+\gamma^2 \tan^2 \zeta}{1+(\gamma/\beta)^2 \tan^2 \zeta} \right], \qquad (8)$$

where we recall that ζ is the angle between the rotation c-axis and the line of sight. With the condition $\Delta m \lesssim 0.01$ imposed by observations[13, 14], and taking the case $\beta=0.771$, $\gamma=0.506$ discussed above (see also Fig. 2), we find that ζ should be smaller than 18 degrees. This has also a low probability of 5% to occur for a randomly oriented rotation axis.

In conclusion, elongated limbs cannot be excluded by our observation, but they require a fast rotating body (period less than ~ 8 hours) outside the interval $R_E=1{,}165\pm 90$ km (Fig. 4S). Moreover, very elongated bodies, for instance with $R_E\sim 1{,}500$ km, require a simultaneous fine tuning on the limb and the rotation axis orientations, and thus does not appear as plausible. We finally note that if a rotational light curve is eventually detected for Eris, then ϵ would then be determined from Eq. 4 or Eqs. 6-7, and Fig. 4S can be used to pin down the value of R_E.

4.4 Constraints from Dysnomia

The satellite is about 60 times fainter than Eris in K' band[36], and 480 times fainter in V band[12]. The satellite spectrum is thus very different from Eris' (and quite redder), suggesting a significantly darker surface.

We may assess an upper limit for Dysnomia's mass by considering a very dark satellite with a visible albedo of ~ 0.05. Then its radius would be $R_D \sim 240$ km (using an estimation of $R_E \sim 1{,}150$ km for Eris' radius), its projected surface area would be $\sim 4\%$ of Eris', and its mass ratio to the primary would reach ~ 0.01 (assuming the same densities for the two bodies). Let us first assume that Dysnomia was formed during a giant impact on Eris and tidally migrated in the primary equatorial plane, from the Roche limit ($\sim 2R_E$) to its present orbit (semi-major axis $\sim 37{,}400$ km, eccentricity lower than 0.01 and period 15.77 days[12]) by extracting orbital angular momentum from the primary rotation. With the maximum mass estimated above, Dysnomia could have decreased Eris' spin rate from a primordial rotation period of ~ 7.5 hours (typical of rotation periods observed among TNOs[37]) to a present period of ~ 11.5 hours.

At this rate, Eris' flattening would be $\epsilon'\sim0.041$ (Eq. 5). However, as the angle between Dysnomia orbital pole (which coincides with Eris' pole in the present scenario) and the line of sight is close to 50 degrees[12], the apparent flattening of Eris' limb in the plane of the sky would be reduced to about 0.024. Also, Eris' rotation axis position angle would then be $P\sim10$ degrees[12]. Using these values, we can fit the occultation chords with an effective radius of $R_E=1{,}143$ km, smaller than the value derived from the circular fit ($R_E=1{,}163$ km).

If we now assume that Dysnomia is much smaller than considered in the extreme case above, but still revolving in Eris' equatorial plane, we still have to fix $P\sim10$ degrees, but we can relax the condition on ϵ'. Using solutions 1 and 2, we then obtain an effective radii R_E in the range 1,105–1,155 km, smaller again than the circular fit value.

Finally, if Dysnomia has been captured and migrated inward to its present orbit[38], then no constraints on Eris' rotational period and pole orientation can be derived, and we have to turn back to the discussion developed in the previous subsection.

4.5 Comparison with Pluto's size

Pluto's radius has been estimated using various techniques, ranging from direct imaging to speckle interferometry, mutual Pluto-Charon events (occultations and eclipses), and stellar occultations[8].

Each of those methods is model-dependent and relies on assumptions on physical parameters that must be independently inferred. Pluto's radius cannot be accurately measured using direct imaging, owing to its small angular diameter, about 0.1 arcsec. Pluto's radius was first pinned down using mutual events observed in the late 1980's, with values ranging from 1,151±4 km (ref. 6) to 1,178±23 km (ref. 7), depending on assumed Charon's orbital radius and Pluto photometric properties[8].

Pluto stellar occultations cannot reach the usual kilometer accuracy level achieved with airless bodies, as Pluto's atmosphere refracts stellar rays. Actually, during occultations, the stellar image is dimmed but always visible, and in particular, is never blocked by Pluto's opaque limb. However, combining stellar occultation results with Pluto atmospheric models, it is possible to estimate a radius value of 1,152±32 km (ref. 3), recently improved to $1{,}180^{+20}_{-10}$ km (ref. 5).

Independent results are obtained with high resolution spectroscopy, which provides constraints on the atmospheric CH_4 integrated column density and temperature, yielding an allowed range of 1,159-1,203 km for Pluto's radius, when combined with stellar occultation results[4].

As those values are obtained with different techniques and assumptions, it is not possible to average them in order to reduce error bars. At the present time, we can only say that Pluto's radius safely lies between $\sim1{,}150$ and 1,200 km. Therefore, it cannot be concluded whether Eris is smaller or bigger than Pluto, until the latter is more precisely measured.

5 Albedo

Eris' geometric albedo p is related to its reflectivity I/F and its radius R_E (now assuming a circular limb with $R_E=1{,}163\pm6$ km) through the equations:

$$(I/F)(\alpha) = \Phi(\alpha) \cdot p = \Phi(\alpha) \cdot (AU_{km}/R_E)^2 \cdot 10^{0.4(H_\odot - H_E)}. \tag{9}$$

Here, $(I/F)(\alpha)$ is the ratio of Eris' surface brightness I observed at phase angle α, to F, the surface brightness of a Lambert surface, where πF is the solar flux density at Eris for the relevant wavelength, $\Phi(\alpha)$ is the phase function (with the convention $\Phi(0)=1$), $AU_{km}=1.49598\times10^8$ is 1 AU expressed in

km, $H_\odot$ is the Sun apparent magnitude (at 1 AU), and H_E is Eris' absolute magnitude, that would be observed if the object were at 1 AU from the Sun and observed at 1 AU from Earth at exact opposition (α=0). In the visible band, ref. 39 provides $H_{E,V}$=-1.116±0.009. We will use here the more recent values $H_{E,V}$=-1.15$^{+0.05}_{-0.1}$ and $H_{E,R}$=-1.56$^{+0.05}_{-0.1}$ in V and R bands, respectively, where the asymmetric error bars come from the analysis of a possible opposition effect (ref. 40 and I. Belskaya 2011, private communication). Finally, using $H_{\odot,V}$=-26.74 and $H_{\odot,R}$=-27.10, we obtain:

$$\begin{cases} p_V = 0.96^{+0.09}_{-0.04} \\[2mm] p_R = 1.01^{+0.10}_{-0.05} \end{cases} \tag{10}$$

Note that the error bars are dominated by the photometric uncertainties attached to $H_{E,V}$ and $H_{E,R}$, not by the uncertainty on R_E. Note also that Eris' phase angle α varies between ~0.15 and 0.6 degrees as seen from Earth, and that the values of $H_{E,V}$ and $H_{E,R}$ given above assume ordinary opposition effect[40]. If Eris has a strongly peaked opposition surge below 0.15 degrees (which is not known), then we would obtain higher geometric albedos than given in Eqs. 10. More generally, a review of TNO and Centaur photometric properties[41] actually shows that the largest TNOs (Eris, Haumea, Makemake and Pluto) have shallower phase slope when compared with smaller TNOs, possibly associated with active (sublimating atmosphere) surfaces and/or collisional history. However, the lack of data at very small ($\lesssim$0.1 degrees) phase angles prevents conclusions to be drawn about the existence of opposition surges for TNOs. An exception is Varuna, for which a surge has clearly been observed at α~0.06-0.1 degrees (ref. 41).

The geometric albedos derived here for Eris can be compared to the visual geometric albedos of Enceladus, p_V~1.4 and Tethys, p_V~1.2 (ref. 20). However, because those satellites exhibits strong opposition surge of more than 30% for $\alpha\lesssim$0.2 degrees, and because Eris' photometric behavior is not known in this domain, we may instead compare their reflectivity $(I/F)(\alpha)$ in the same range of phase angle. For instance, Eris has I/F~0.91 near α=0.15 degrees in visual band[40], while Enceladus has I/F~1.2 in the same conditions[42], about 30% larger than for Eris.

6   Surface temperature

We now use the radius R_E and the geometric albedo p_V derived above, in combination with thermal fluxes at 70 and 1,200 μm (measured by *Spitzer*[22] and *IRAM*[11], respectively), to constrain Eris' surface temperature and global photometric properties. We consider two limiting cases: (1) slow rotation (or equivalently, pole-on orientation, or equivalently, zero thermal inertia), referred to as the 'Standard Thermal Model' (STM) and (2) fast rotation with equator-on geometry and Isothermal Latitude Model (ILM). The first model provides the 'warm' equilibrium situation, where only the illuminated side of Eris is heated by the Sun, while the second model yields the 'cool' situation, where the temperature is constant along a given latitude (on both the lit and unlit sides). Actual models should lie between these extreme cases.

In each model, we use the formulae in Table 4S to calculate the sub-solar temperature T_{ss} for the STM and the equatorial temperature T_{eq} for the ILM. In that table, the angle θ is the local solar zenith angle (STM) and ϕ is the local latitude (ILM). The local temperature T given in the first line is introduced in the integral of the second line in Table 4S. This yields T_{ss} (STM) and T_{eq} (ILM), introducing the emissivity ε (not to be confused with the flattening ϵ defined earlier) and using Planck's law B_ν, once Eris' flux density S_ν at frequency ν and geocentric distance Δ is measured (note that Δ=96.28 UA for the *IRAM* data and Δ=96.41 UA during the *Spitzer* observations). In the calculations, we neglect Dysnomia's contribution to the total thermal flux, as its projected surface area is probably more than 25 times smaller than Eris', see above.
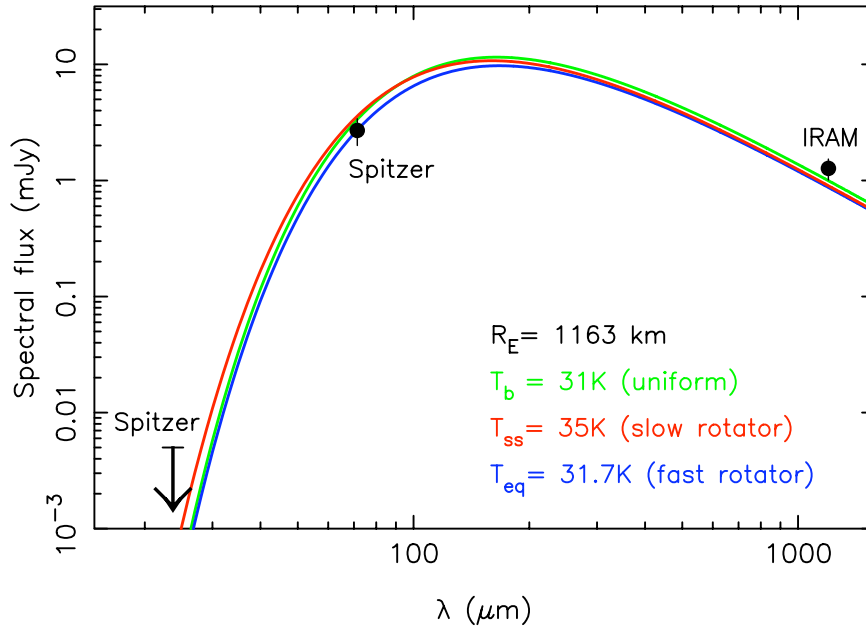
Figure 5S | Eris thermal models. The observed Eris' thermal fluxes near 70 and 1,200 μm (see Table 5S and refs. 11,22) in millijansky are compared to various models discussed in the text, assuming a radius R_E=1,163 km and a standard emissivity[22] ε=0.9 for the dwarf planet. Note that only an upper limit is available at 24 μm (arrow). Green: expected flux from a black body with uniform brightness temperature T_b=31 K. Red: expected flux using a Standard Thermal Model (STM), or slow rotator, with a sub-solar temperature T_{ss}=35 K. Blue: expected flux using a Isothermal Latitude Model (ILM), or fast rotator, with an equatorial temperature T_{eq}=31.7 K. All models agree to within 1.5σ or better with the 70 and 1,200 μm measurements, and thus describe satisfactorily the data.

Supplementary Table 4S | Formulae to calculate temperatures

slow rotator (STM)	equator-on fast rotator (ILM)
$T = T_{ss} \cdot \cos^{1/4}(\theta)$	$T = T_{eq} \cdot \cos^{1/4}(\phi)$
$S_\nu = \pi\varepsilon \left(\frac{R_E}{\Delta}\right)^2 \cdot \int_0^{\pi/2} \sin(2\theta) B_\nu\left[T(\theta)\right] d\theta$	$S_\nu = 2\varepsilon \left(\frac{R_E}{\Delta}\right)^2 \cdot \int_{-\pi/2}^{\pi/2} \cos(\phi)^2 B_\nu\left[T(\phi)\right] d\phi$
$T_{ss} = T_0 \cdot \left[(1 - p_V q)/(\varepsilon\eta)\right]^{1/4}$	$T_{eq} = T_0 \cdot \left[(1 - p_V q)/(\pi\varepsilon\eta)\right]^{1/4}$

$$S_\nu = \pi \left(\frac{R_E}{\Delta}\right)^2 \cdot B_\nu\left(T_b\right)$$

The third line of Table 4S provides the thermal equilibrium equations that relate T_{ss} and T_{eq} to Bond's albedo $A=p_V q$, where p_V is the geometric albedo in visible band (where most of the solar flux is emitted), q is the phase integral and η is the beaming factor describing the effects of surface roughness (which enhance the thermal radiation at low phase angles), following the NEATM[43] and Hybrid STM/ILM formalisms[22]. The quantity T_0 is the equilibrium sub-solar temperature of a perfectly diffusing and completely absorbing surface with unit emissivity at Eris distance, $T_0=[F_\odot(r)/\sigma_{SB}]^{1/4}$, where $F_\odot(r)$ is the solar flux integrated over all wavelengths at distance r from the Sun, and σ_{SB}=5.670×10^{-8} W m^{-2} K^{-4} is the Stefan-Boltzmann constant. Using $F_\odot$(1 AU)=1367 W m^{-2}, and r=96.9 AU, we obtain T_0=40.0 K. Solutions in terms of T_{ss} and T_{eq} are found in Table 5S.

Finally, the fourth line of Table 4S relates the flux density S_ν to the disk-averaged brightness temperature T_b of the dwarf planet, i.e. the temperature of a perfect black body with Eris' size that would emit the flux density S_ν toward the observer.

Supplementary Table 5S | Thermal fluxes and temperature constraints for a 1,163 km radius

Wavelength (μm)	Flux (mJy)	Tb (K)[a]	Slow rotator T_{ss} (K)[a]	Fast rotator T_{eq} (K)[a]
23.68	< 0.005 (*Spitzer*)[b]	< 37.2	< 40.2	< 38.6
71.42	2.7±0.7 (*Spitzer*)[b]	30.0±1.2	33.5±1.4	31.7±1.3
1,199	1.27±0.26 (*IRAM*)[c]	38.0±7.5	46.8±9.3	43.6±8.7

[a] The error bars on temperature are dominated by errors on the fluxes, not on our radius determination.
[b] From ref. 22.
[c] From ref. 11.

In the slow rotation model, the 70 μm flux is fit with a sub-solar temperature T_{ss}=33.5±1.4 K, while the 1,200 μm flux gives T_{ss}=46.8±9.3 K. A satisfactory compromise, matching both the *Spitzer* and *IRAM* measurements close to their respective 1σ error bars, is achieved for T_{ss}∼35 K (Fig. 5S). In the fast rotation model, the 70 μm flux implies T_{eq}=31.7±1.3 K, that satisfactorily fits the 70 and 1,200 μm data (Fig. 5S).

Finally, our occultation measurement provides the geometric albedo p_V=0.96$^{+0.09}_{-0.04}$. Adopting a standard value ε=0.9 (ref. 22), the only two free model parameters are η and q in the third line of Table 4S. Using the STM, i.e. T_{ss}∼35 K and a plausible range from η=1 (no roughness) to 0.7 (large surface roughness), leads to q=0.49-0.66, which is fully consistent with Saturn's brightest icy satellites Mimas, Enceladus, Tethys, Dione and Rhea (q = 0.51-0.63), as inferred from their geometric and bolometric albedos[20, 23], see main text.

The ILM in contrast leads to extreme conditions for q. Even at the lower possible value T_{eq}=31.7 K and with 0.9>η>0.7, we obtain 0<q<0.24, an implausible range as bright objects also have large phase integrals[24]. The situation is even worse if we note that the lower bound of 0.7 for η is actually unrealistic in the absence of diurnal temperature variations[44].

7 Limit on atmosphere

Eris' atmosphere, if any, should be composed mainly of nitrogen N_2 (or possibly argon Ar), plus traces of methane CH_4 (ref. 1). However, the atmospheric thermal structure is unknown. If the abundance of methane in Eris' atmosphere is similar to that of Pluto (∼0.5 %, ref. 4), then absorption of near-IR solar radiation by CH_4 may raise the upper atmosphere temperature. In this case, a rough estimate of Eris' upper atmosphere temperature can be simply obtained from the methane 'thermostat-model', in which near-IR heating is balanced through emission in the 7.7 μm methane band[45]. With an incoming solar flux at Eris ten times weaker than at Pluto, this model predicts an Eris' upper atmosphere temperature of 94 K (vs 106 K for Pluto). Then, a 'Pluto-like' thermal profile would start near 30 K at the surface, and ramp up in a few kilometers-thick stratosphere to an isothermal branch at 94 K in the upper atmosphere. Note that the Pluto thermostat-model[45] assumes an optically thin atmosphere. Although more detailed models[46] show this not to be the case, the optically thin approach still provides the correct upper atmosphere temperature, validating the above scaling approach.

However, a 0.5% CH_4 atmospheric abundance is unlikely for Eris. At Pluto, the elevated abundance (compared to expectations based on vapor pressure equilibrium in an ideal N_2-CH_4 mixture) is best interpreted as resulting from the presence of patches of pure, 'warm', methane ice. Those patches are thought to be warmer than nitrogen ice by up to 10-15 K because the N_2 temperature is largely controlled by latent heat flux of a ∼10-μbar atmosphere, large enough to buffer an isothermal N_2 frost

and a spatially uniform atmospheric pressure. This is not the case for Eris, where the atmosphere is presently at least 3 orders of magnitudes more tenuous than on Pluto, so that the local N_2 ice temperature should be driven by local insolation conditions, not by sublimation/condensation processes.

The dominant role of the latent heat flux over thermal flux in establishing the temperature of N_2 can be expressed through the dimensionless parameter $I=L\dot{m}/\sigma_{SB}T^4=Lf_rP/(c_s\sigma_{SB}T^4)$ where L is the sublimation latent heat, $\dot{m}$ the sublimation mass flux, P the atmospheric pressure, c_s the speed of sound, and f_r is the fractional pressure difference between the saturated and actual atmospheric pressure[47]. For large values of I, sublimation processes dominate the local energy flux from the Sun (insolation) and the ice is forced to be isothermal. With the conditions prevailing at Pluto, one obtains $I=5,200$, using a typical $f_r\sim0.1$ (ref. 47). At Eris, using a maximum pressure of ~5 nbar, and $T=30$ K, we obtain $I\lesssim 2$, showing that the latent heat flux is at most comparable to the thermal radiation flux from the surface.

Hence, the surface temperature of a N_2 ice is likely to be primarily driven by local insolation conditions. In particular, our predicted sub-solar temperature is at least 32 K (Table 5S), which corresponds to a N_2 equilibrium vapor pressure[48] larger than 260 nbar, much higher than the upper limit derived here. Consequently, a local N_2 atmosphere might exist at Eris' sub-solar point, and that atmosphere could freeze out to undetectable levels (less than a few nbars) at the limb and on the night side, as it is the case for Io[49]. Detailed models will be required to confirm this point.

Note that if there are regions covered by pure methane ice on Eris, they should not be significantly warmer than N_2. The bulk methane abundance on Eris' surface[1], 10%, is similar to the solubility limit of CH_4 in N_2 (ref. 50), suggesting the formation of pure ice grains. Assuming that such pure CH_4 ice grains exist but are at the same temperature as N_2, the atmospheric CH_4/N_2 is given by the ratio of their vapor pressures at ~30 K, i.e. a few times 10^{-5} at most. If pure methane grains are not present and the CH_4/N_2 surface ratio is 10 %, the atmospheric CH_4/N_2 is further decreased by a factor 10.

We conclude that the probable range of methane abundance in Eris' atmosphere is 10^{-5}–10^{-6}. Although detailed models would be needed, this is likely unsufficient to lead to a significant stratosphere, and we favor the case where any Eris' atmosphere is isothermal near ~30 K. More precisely, when considering such atmospheres, we have assumed that the pressure at the surface corresponds to the saturation value at a given temperature[48]. We have generated synthetic light curves (see Fig. 3) caused by a tenuous atmosphere using a ray tracing code, as detailed in ref. 29. Assuming a N_2 isothermal atmosphere near 30 K, we derive an upper limit of about 1 nbar (1σ limit), see Fig. 3. Assuming a Pluto-like atmosphere (30 K near the surface and 94 K in the upper atmosphere), we would obtain upper limits larger by a factor of 3-4 compared to the isothermal model.

We can also place upper limits of about 1 nbar for isothermal pure methane or pure argon atmospheres. In order to sublimate at that pressure[48], the methane ice should be at about 37 K. As our surface temperature estimates are comparable to or smaller than those values, it is normal that a CH_4 atmosphere escaped detection.

Finally, we note that Eris, if indeed covered by N_2 ice, might develop an atmosphere as it approaches perihelion, at 37.8 AU. In that case, the N_2 ice temperature will be buffered by the nitrogen atmosphere, implying a constant temperature on night and day sides. Assuming a maximum Bond albedo of 0.7 (typical of bright objects like Enceladus[23]), we expect a surface equilibrium temperature of at least ~35 K, large enough to maintain a 2 μbar or more Pluto-like atmosphere. This atmosphere might collapse when Eris recedes from perihelion, thus explaining its current bright surface caused by a thin nitrogen-ice coating.

References

27. Jehin, E. *et al.* TRAPPIST : TRAnsiting Planets and PlanetesImals Small Telescope. *The Messenger* **145**, 2–6 (2011).

28. van Belle, G. T. Predicting Stellar Angular Sizes. *Publ. Astron. Soc. Pacific* **111**, 1515–1523 (1999).

29. Widemann, T. *et al.* Titania's radius and an upper limit on its atmosphere from the September 8, 2001 stellar occultation. *Icarus* **199**, 458–476 (2009).

30. Giorgini, J.D. *et al.* JPL's on-line solar system data service. *Bull. Am. Astron. Soc.* **111**, 1158 (1996).

31. Lellouch, E., Hubbard, W.B., Sicardy, B., Vilas, F. & Bouchet, P. Occultation determination of Neptune's oblateness and stratospheric methane mixiong ratio. *Nature* **324**, 227–231 (1986).

32. Johnson, T.V. & McGetchin, T.R. Topography on Satellite Surfaces and the Shape of Asteroids. *Icarus* **18**, 612–620 (1973).

33. Schenk P. & and Jackson, M.P.A. Diapirism on Triton: A record of crustal layering and instability. *Geology* **21**, 299–302 (1993).

34. Plummer, H. C. On the ellipticities of the Maclaurin ellipsoids. *Mon. Not. Roy. Astron. Soc.* **80**, 26–33 (1919).

35. Binzel R., Farinella P., Zappala V. & Cellino A. in *Asteroids II* (eds Binzel, R. P., Gehrels, T. & Matthews, M.S) 416–441 (Univ. Arizona Press, Tucson 1989).

36. Brown, M.E. S/2005 (2003 UB) 1 *Central Bureau for Astronomical Telegrams*, Circular No. 8610 (2005).

37. Duffard, R., Ortiz, J. L., Thirouin, A., Santos-Sanz, P. & Morales, N. Transneptunian objects and Centaurs from light curves. *Astron. Astrophys.* **505**, 1283–1295 (2009).

38. Greenberg, R. & Barnes, R. Tidal evolution of Dysnomia, satellite of the dwarf planet Eris. *Icarus* **194**, 847–849 (2008).

39. Rabinowitz, D.L., Schaeffer, B.E. & Tourtelotte, S. W. The Diverse Solar Phase Curves of Distant Icy Bodies. I. Photometric Observations of 18 Trans-Neptunian Objects, 7 Centaurs, and Nereid. *Astron. J.* **133**, 26-43 (2007).

40. Belskaya, I. N. *et al.* Polarimetry of the dwarf planet (136199) Eris. *Astron. Astrophys.* **479**, 265-269 (2008).

41. Belskaya I.N., Levasseur-Regourd A.-C., Shkuratov Yu.G., Muinonen K. in *The Solar System Beyound Neptune* (eds Barucci, M.A., Boehnhardt, H., Cruikshank, D.P. & Morbidelli, A.) 115–127 (Univ. Arizona Press, Tucson, 2008).

42. Verbiscer, A., French, R. G. & McGhee, C. A. The opposition surge of Enceladus: HST observations 33–1022 nm. *Icarus* **173**, 63–83 (2005).

43. Harris A. W. A thermal model for near-Earth asteroids. *Icarus* **131** 291–301 (1998).

44. Spencer, J. R. A Rough-Surface Thermophysical Model for Airless Planets. *Icarus* **83**, 27–38 (1990).

45. Yelle, R. V. & Lunine, J. I. Evidence for a molecule heavier than methane in the atmosphere of Pluto. *Nature* **339**, 288–290 (1989).

46. Strobel, D.F., Zhu, X., Summers, M.E. & Stevens, M.H. On the Vertical Thermal Structure of Pluto's Atmosphere. *Icarus* **120**, 266–289 (1996).

47. Stansberry, J. *et al.* A model for the overabundance of methane in the atmospheres of Pluto and Triton *Planet. Space Sci.* **44**, 1051-1063 (1996).

48. Fray, N. & Schmitt, B. Sublimation of ices of astrophysical interest: a bibliographic review. *Planet. Space Sci.* **57**, 2053-2080 (2009).

49. Trafton, L.M., Matson, D.L. & Stansberry, J.A. in *Solar System Ices* (eds Schmitt, B., de Bergh, C. & Festou, M.) 773–812 (Kluwer Academic Publishers, Boston, 1998).

50. Prokhvatilov, A. I. & Yantsevich, L. D. X-ray investigation of the equilibrium phase diagram of $CH_4 - N_2$ solid mixture. *Sov. J. Low Temp. Phys.* **9**, 94-98 (1983).